IOP Publishing Measurement Science and Technology
Meas. Sci. Technol. **30** (2019) 105701 (9pp) https://doi.org/10.1088/1361-6501/ab23e7

Methods for characterization and optimisation of measuring performance of stereoscopic x-ray systems with image intensifiers

J G Sanctorum[1], D Adriaens[2], J J J Dirckx[1], J Sijbers[3], C Van Ginneken[4], P Aerts[5,6] and S Van Wassenbergh[5,7,8]

[1] Department of Physics, Laboratory of Biophysics and Biomedical Physics, University of Antwerp, Groenenborgerlaan 171, 2020 Antwerpen, Belgium
[2] Evolutionary Morphology of Vertebrates, Ghent University, K L Ledeganckstraat 35, 9000 Gent, Belgium
[3] Department of Physics, Imec-Vision Lab, University of Antwerp, Universiteitsplein 1, 2610 Antwerpen, Belgium
[4] Department of Veterinary Sciences, Laboratory of Applied Veterinary Morphology, University of Antwerp, Universiteitsplein 1, 2610 Antwerpen, Belgium
[5] Department of Biology, Laboratory of Functional Morphology, University of Antwerp, Universiteitsplein 1, 2610 Antwerpen, Belgium
[6] Department of Movement and Sport Sciences, Laboratory of Biomechanics and Motor Control of Human Movement, Ghent University, Watersportlaan 2, 9000 Gent, Belgium
[7] Département Adaptations du Vivant, UMR 7179 C.N.R.S/M.N.H.N., 57 rue Cuvier, Case Postale 55, 75231 Paris Cedex 05, France

E-mail: sam.vanwassenbergh@uantwerpen.be

Received 7 December 2018, revised 29 April 2019
Accepted for publication 22 May 2019
Published 8 August 2019

Abstract

The use of biplanar high-speed x-ray fluoroscopy to study fast, 3D movements that are inaccessible from external views has grown significantly in the past decade. Owing to the development of specialised software for calibration, distortion correction, and automated tracking of radio-opaque marker implants, this technique will soon become the standard to analyse skeletal kinematics of vertebrate animals. However, tests of important characteristics of biplanar x-ray systems, such as resolution and precision, remain scarce and incomplete. We present methods to determine imaging resolution and 3D stereoscopic and dynamic resolutions to follow moving markers in 3D, and demonstrate them on a newly installed stereoscopic x-ray system with image intensifiers. Using four-megapixel cameras, image resolution slightly surpasses previous reports. The spatial resolution appears to be optimal at magnification factors (ratio of source-to-detector to source-to-subject distance) between 1.33 and 2.20. This new information will allow biplanar x-ray system users to optimise the relative position of tube, subject, and image intensifiers.

Keywords: kinematics, XROMM, cineradiography, fluoroscopy, resolution, precision

Supplementary material for this article is available online

(Some figures may appear in colour only in the online journal)

[8] Author to whom any correspondence should be addressed.

Introduction

Videos from biplanar x-ray systems are becoming increasingly popular to analyse three-dimensional (3D) motion, especially within the field of biomechanics (Brainerd *et al* 2010, Camp *et al* 2016, Orsbon *et al* 2018). Since the analogue x-ray image intensifiers of such biplanar x-ray video systems typically show a persistence of luminescence after x-ray stimulation of only about 1 ms (Wang and Blackburn 2000), digital high-speed cameras are generally used to record the image intensifier's output screen at high frame rate (Snelderwaard *et al* 2002). During the last two decades, synchronised, high-speed, biplanar x-ray videos have been used to unravel the 3D kinematics of a variety of behaviors in a wide range of vertebrate animals, such as limb bone movement of horses during locomotion (e.g. Geiger *et al* (2018)), vertebral movement during running in dogs (Wachs *et al* 2016), movement of the skeleton and strain in tendons of wings of flying bats (Konow *et al* 2015), and muscle contractions and head expansions during suction feeding in fishes (Camp and Brainerd 2014).

Biplanar x-ray videography owes a significant part of its popularity in the field of biomechanics to the pioneering work at Brown University, where a user-friendly workflow was developed to accurately reconstruct 3D motions of skeletal elements in professional 3D animation software (Brainerd *et al* 2010, Gatesy *et al* 2010). This workflow is known as x-ray reconstruction of moving morphology (XROMM), and includes software and protocols to calibrate, remove distortion artefacts, automatically track radio-opaque markers, and animate and analyse relative movements. The ability to check the calibration error in less than 1 min prior to a recording session, as well as the strongly reduced time for kinematic data extraction due to free and open-source software XMALab (Knörlein *et al* 2016), significantly increases the success of biplanar x-ray videography as a research tool.

However, little information is present on the performance of these systems which are fast gaining in popularity. Quantifications of resolution and accuracy have thus far only been reported for the system at Brown University (e.g. Brainerd *et al* (2010) and Miranda *et al* (2011)). In this article, we present methods to quantify performance of a stereoscopic high-speed x-ray setup and we demonstrate them using a newly installed biplanar x-ray video system (figure 1) that is equipped with the latest generation of high-speed cameras (4 megapixel resolution; 2048 × 2048 pixels), and Brown University's XMALab software for marker tracking (Knörlein *et al* 2016). We also provide the first tests of how the spatial resolution varies in function of the position of the object between source (i.e. the focal spot of the emitted x-rays) and the detector (i.e. the image intensifier's scintillator layer) for such a high-speed system. This is important since placing the object away from the image intensifier is always required when recording in a biplanar configuration.

Methods

Equipment

The biplanar x-ray video system at the University of Antwerp, named 3-dimensional dynamic morphology using x-rays ($3D^2YMOX$) (figure 1), was constructed by RSTmedical (Oirschot, The Netherlands) and consists of the following components: a Philips Super CP80 (80 kW; 40 to 125 kV) x-ray power generator (Koninklijke Philips NV, Eindhoven, The Netherlands) with two controller units; rotating tungsten anode Philips SRM 0511 x-ray tubes with Philips XD6028 collimators, attached by Arco Ceil motorised ceiling stands (Arcoma AB, Vägjö, Sweden); two Philips Imagica HC 38 cm diameter image intensifiers mounted on a RSTmedical image intensifier trolley, each fitted with a Philips XTV11 monitoring camera, and a Photron FastCam Mini WX50-32 GB high-speed camera (10 μm pixels CMOS sensor; Photron Inc., San Diego, USA) with a Samyang 85 mm *f*/1.4 lens (Samyang Optics Company Limited, Masan, South Korea). X-rays can be generated from a small focal spot ($f = 0.5$ IEC 336/1993; measured as 0.5 mm by 0.8 mm on supplied pinhole radiograms) or a larger focal spot ($f = 1.1$ IEC 336/1993; measured as 1.2 mm by 1.8 mm on supplied pinhole radiograms). The image intensifiers can be set to either a large, medium, or small field of view. The resolution in the centre of the Philips Imagica HC 38 as measured by the constructor on 100 mm film is 3.1, 4.0 and 5.6 lp mm^{-1} for the large, medium, and small field of view, respectively. Frames from the two high-speed cameras are synchronised in a master-slave configuration, and controlled by Photron Fastcam Viewer software.

Imaging optimisation

Twelve-bit grayscale images (the current standard for high-speed CMOS cameras) were recorded at the highest frame rate (750 Hz) for full pixel resolution (2048 × 2048 pixels) of the high-speed cameras. In order to reduce the variation in illumination intensity across the images, a 'pixel gain correction' was performed prior to the recording sessions. To do so, an empty scene was recorded at x-ray settings reaching subsaturation read-outs of the sensor for about 2 s, after which the Photron software adjusted gains for the sensor's pixels. This calibration procedure creates a flat-fielded image, which improves the dynamic range of the system (figure 2).

Calibration and distortion correction

Three-dimensional volumes were calibrated using a Lego cube phantom that includes 64 steel spheres (diameter 0.5 mm) at known positions, and four symbols made out of soldering wire to determine the position of a Cartesian reference frame. The geometry and construction guide of this

Figure 1. Biplanar x-ray video set-up at the University of Antwerp. Note that the x-ray sources (tubes) and beam collimators are attached to ceiling rails, while the image intensifiers and attached cameras are mounted on trolleys. The four main units (two sources and two detectors) are height adjustable and tiltable to allow for different beam orientations.

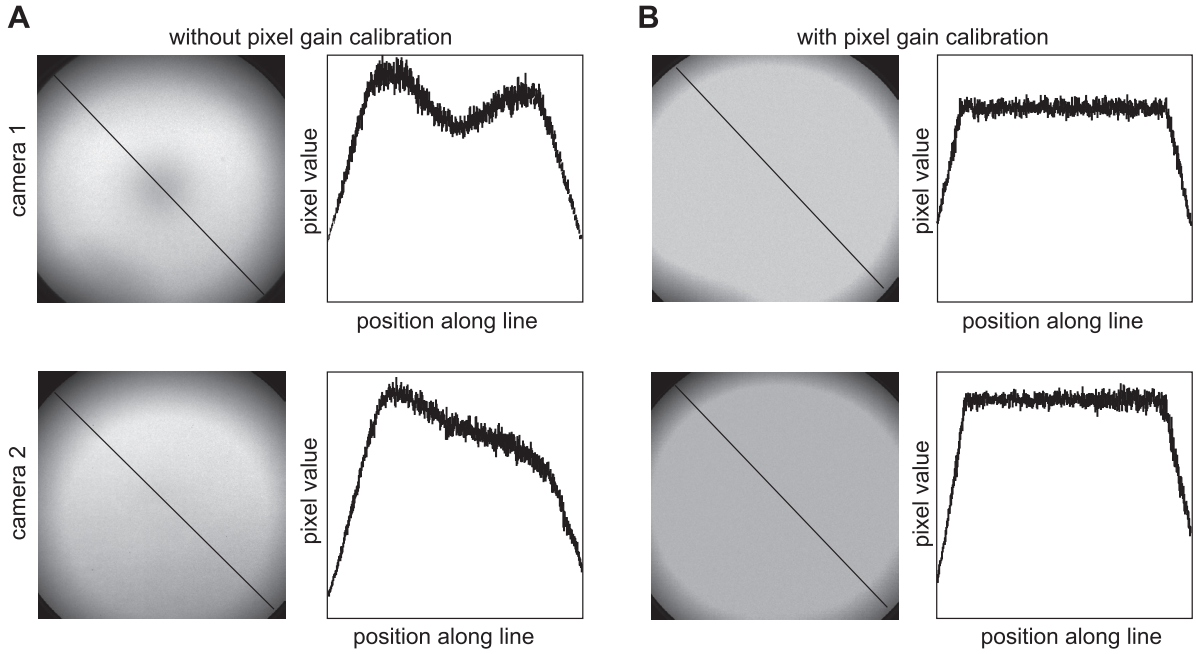

Figure 2. Effect of pixel gain calibration of the Photron high-speed camera sensor on spatial variation of grey values across the image. Without this calibration (A), a significant variation in pixel readout values exists for empty scenes. The pattern differs among the individual image intensifiers, as shown by the difference in the images of camera 1 (top row) and camera 2 (bottom row). After performing the pixel gain calibration (B), a 'flat' image is achieved except on the outer edges. In addition to the heel effect, which causes slightly higher illumination at the side where the tube's cathode is located (top in figure), local variation and asymmetry in illumination can be due to non-uniformity of the scintillator layer of the image intensifier's input screen.

phantom is provided as supplementary information with the publication by Knörlein *et al* (2016). X-ray images of perforated aluminum plates with hole diameters of 3 mm, spacing between the hole centres of 5 mm, and a total thickness of 2 mm (two R3T5 1 mm plates; Aluminium Op Maat Gemaakt BVBA, Herentals, Belgium) placed parallel against the front of the image intensifiers were used to compute the distortion corrections in XMALab 1.5.1.

Measuring resolution

Spatial resolution was measured with a line pair phantom (Leeds resolution pattern number 38; Leeds Test Objects Ltd North Yorkshire, UK). This phantom contains triple slits with 20 samples of spacing between 0.6 and 5.0 line pairs (lp) per mm (figure 3). Resolution was quantified in two ways: (1) *visually distinguishable resolution* was defined as the smallest

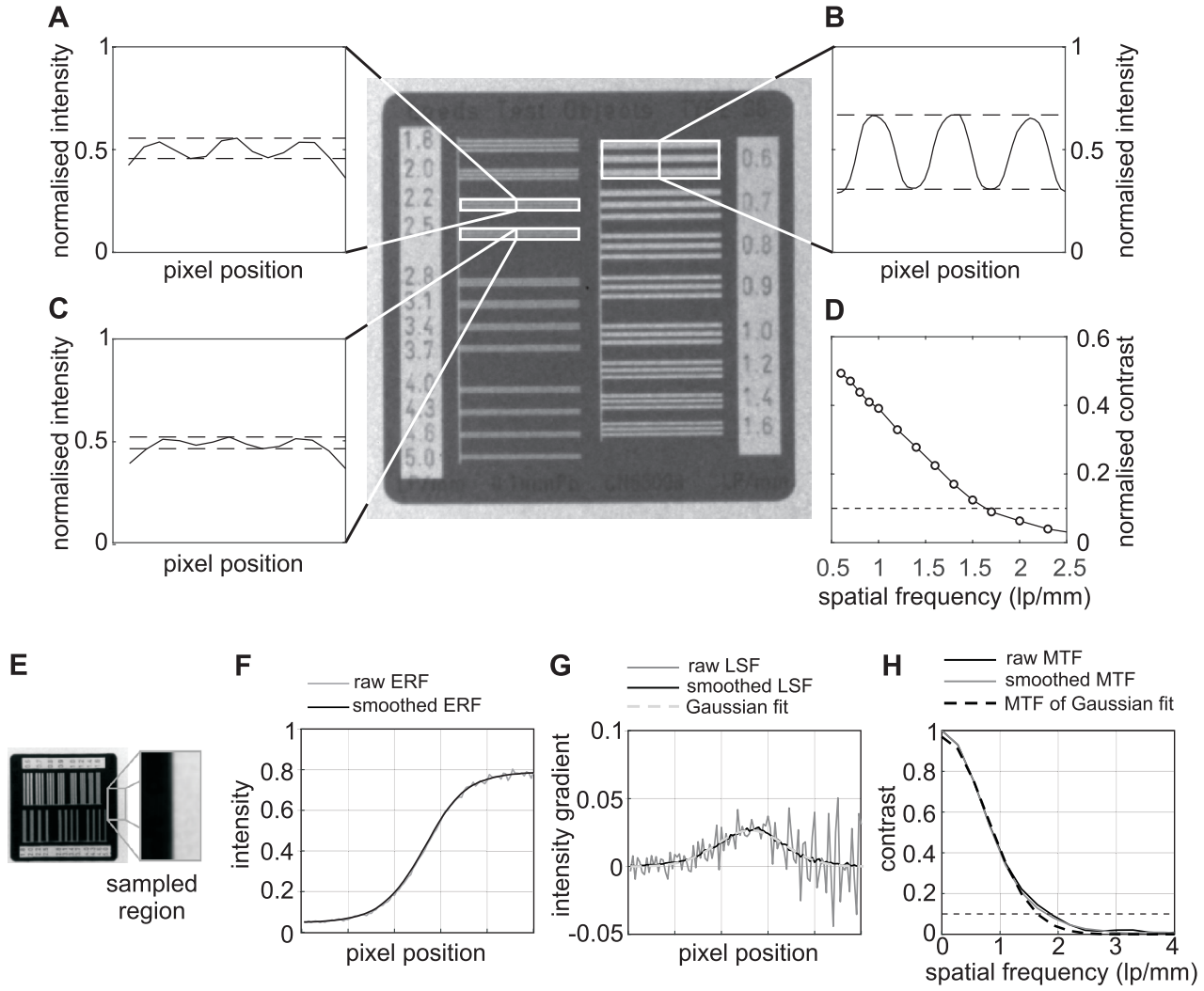

Figure 3. Measurement of the spatial resolution using the leeds test object. The two approaches for determining modulation transfer function (MTF) are illustrated in, respectively, (A)–(D) (line-pattern-based approach) and (E)–(G) (edge-based approach). The white rectangles depict the subsets over which the normalised contrast was averaged. In (A), the line profile for a spatial frequency of 2.2 lp mm^{-1} is shown, for which the MTF nearly reaches 10%. In (B), the line profile for 0.6 lp mm^{-1} is shown. Figure (C) shows the line profile for a spatial frequency of 2.5 lp mm^{-1}, for which the MTF is lower than 10%, but contrast is still visually distinguishable. In (D), the MTF is sampled by reading out the line profiles and averaging over the selected region. The horizontal dashed line depicts the 10% MTF criterion. In (E), the edge region analysed in the panels on its righthand side is displayed. This analysis includes the extraction of an averaged edge response function over the image region (raw and smoothed) (F), deriving the raw and smoothed ERF to obtain the raw line spread function (LSF), smoothed LSF and a Gaussian fit of the smoothed LSF (G), and using the MTFs computed via FFT (H) from the raw, smoothed and Gaussian fitted LSF to determine the 10% MTF resolution (crossing with the horizontal dashed line).

triple-slit spacing (i.e. highest lp mm^{-1}) for which a triple-spike profile could be measured on a line transect perpendicular to the slits on the digital image of the phantom. (2) *10% MTF resolution* was calculated. To do so, the modulation transfer function (MTF) was sampled experimentally. The MTF describes the relation between the normalized contrast and the corresponding spatial frequency of the line pattern. The 10% MTF resolution corresponds to the drop of the normalised contrast (or MTF) to 10% (Du *et al* 2007, Bushong 2017). The 10% MTF threshold crossing was calculated using shape-preserving piecewise cubic interpolation (Yang and Huiyan 1996).

Two approaches were used to derive MTFs. First, the line pair patterns gradings of the Leeds phantom were used (figures 3(A)–(D)). In this approach, the normalised contrast (C_n) was calculated as the ratio of the contrast between the lines (C) and maximum contrast within the image signal (C_0):

$$C_n = \frac{C}{C_0}, \text{with } C = \frac{\max(I_{lines}) - \min(I_{lines})}{\max(I_{lines}) + \min(I_{lines})}, \text{and}$$
$$C_0 = \frac{\max(I_{signal}) - \min(I_{signal})}{\max(I_{signal}) + \min(I_{signal})}, \quad (1)$$

in which max(I_{lines}) and min (I_{lines}) are the maximum and minimum gray values on a line transect perpendicular to the slits of the test object (figures 3(A)–(C)), and max(I_{signal}) and min (I_{signal}) the maximum and minimum gray values over the entire phantom and near surroundings. The normalised intensity ($I_n(x, y)$) used for visualisation purposes (figures 3(A)–(C)) was calculated as

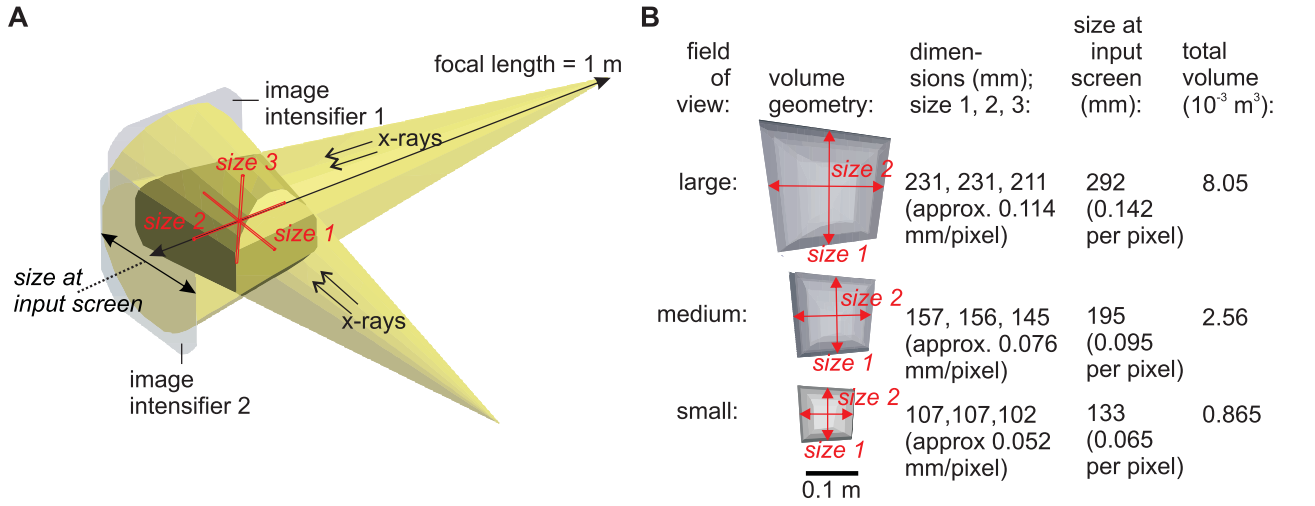

Figure 4. Geometric properties of the imaged 3D volume in a configuration with the image intensifiers placed perpendicularly with respect to each other at 1 m from the focal spot of the x-ray tubes (A). Dimensions at the three selectable fields of view (magnification modes of the image intensifiers) are given in (B). The distance between the centre of the imaging volume and the image intensifier screen is 0.2 m, which corresponds for a magnification factor (i.e. source-detector distance divided by source-object distance) of 1.25. Note that the dual-beam intersection zone forms a complexly shaped 3D volume that is about 10% larger than a sphere with diameters corresponding to the mean of sizes 1, 2, and 3.

$$I_{\mathrm{n}}(x,y) = \frac{I(x,y) - \min(I)}{\max(I) - \min(I)}. \qquad (2)$$

For each of the line transects belonging to the same set (according to a certain spatial frequency), the normalised contrast was calculated using equation (1) and averaged over the set to obtain a mean normalised contrast corresponding to a certain spatial frequency.

Second, spatial resolution was also determined using a more commonly applied method, where the MTF is calculated by measuring the edge response function (ERF) and taking the fourier transform of its derivative, the line spread function (LSF). This method was applied as reported by Judy (1976) and Samei *et al* (1998). A small adjustment was made to their analysis procedure to incorporate the magnification factor in the fast fourier transform (FFT). To measure the ERF, the same Leeds test object was used, since it contains sharp edges (figure 3(E)). An average 1D ERF is calculated over this region and smoothed using a boxcar convolution kernel of height 0.1 and length of 10 pixels (figure 3(F)). The LSF is calculated from both the raw ERF and the smoothed ERF using numerical differentiation, and a Gaussian is fitted to the smoothed LSF (figure 3(G)). For the raw, smoothed and Gaussian fitted LSF, the MTF is calculated using FFT (figure 3(H)). The average of the 10% MTF resolution from these three curves is used in all further analyses. The spatial resolution in vertical direction was calculated by taking the mean of the spatial resolutions obtained by measuring the ERF at the top and bottom side of the phantom. Left and right sides were used to obtain the horizontal spatial resolution.

Table 1. 10% edge-based MTF resolution for the three fields of view.

Image intensifier	Field of view	R_{h} (lp mm^{-1})	R_{v} (lp mm^{-1})
1, 2	Large	1.61, 1.74	1.77, 1.72
1, 2	Medium	2.27, 2.14	2.01, 2.34
1, 2	Small	3.19, 2.82	3.15, 2.44

R_{h} = horizontal resolution, R_{v} = vertical resolution.

Measuring precision

Precision was calculated as the variation of the calculated distance between two markers (lead-tin spheres of 0.5 mm diameter) attached to a rigid object moving through the monitored volume. To do so, the marked object was tied to a rope close to its centre of gravity and was swung and rotated while recording 2.6 s of biplanar video (2000 frames per camera).

Results

Measurement volumes

The volume in view of the two detectors was determined for a standard configuration: the minimal recommended source-to-detector distance of 1 m; two image intensifiers at a 90° angle while leaving 5 cm of spacing to place the perforated grids to correct for geometric distortion. In that case, the centre of the in-view volume was at 20 cm from the front screen of the image intensifier (i.e. the anti-scatter grid), which corresponds to a magnification factor (source-to-detector distance

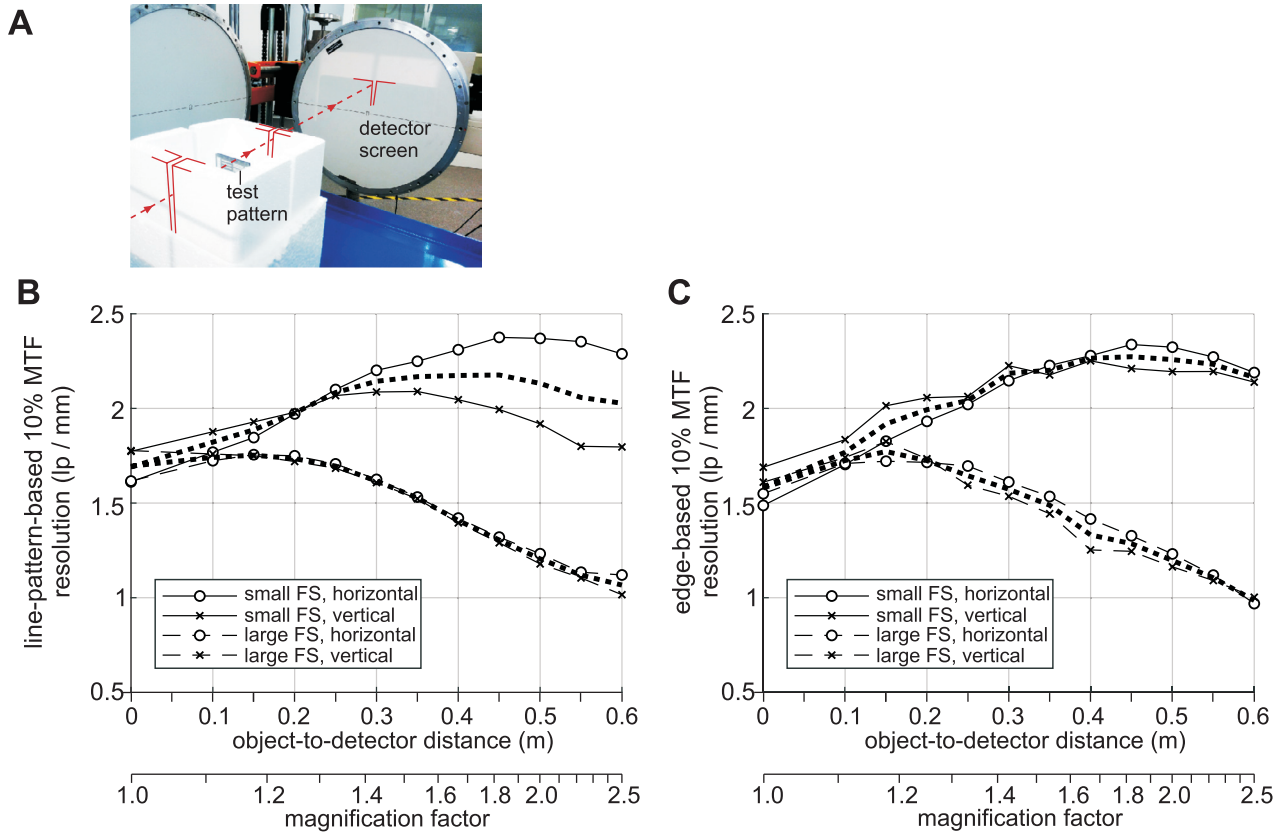

Figure 5. Effect of object-to-detector distance on image resolution. (A) Experimental set-up used to place the test pattern parallel to the detector screen and perpendicular to the x-ray beam by aligning two slits (outlined in red) using light emitted from the x-ray source. (B) Line-pattern-based 10% MTF resolution, and (C) edge-based 10% MTF resolution results for a source-to-detector distance of 1 m for the two focal spot settings of the x-ray tubes for the two different focal spots (FS) and direction on the image (horizontal and vertical). Thick dotted lines represent the square root of the product of horizontal and vertical resolution for a certain focal spot size, yielding a measure for 2D spatial resolution. Magnification factor is defined as source-to-detector distance divided by source-to-object distance.

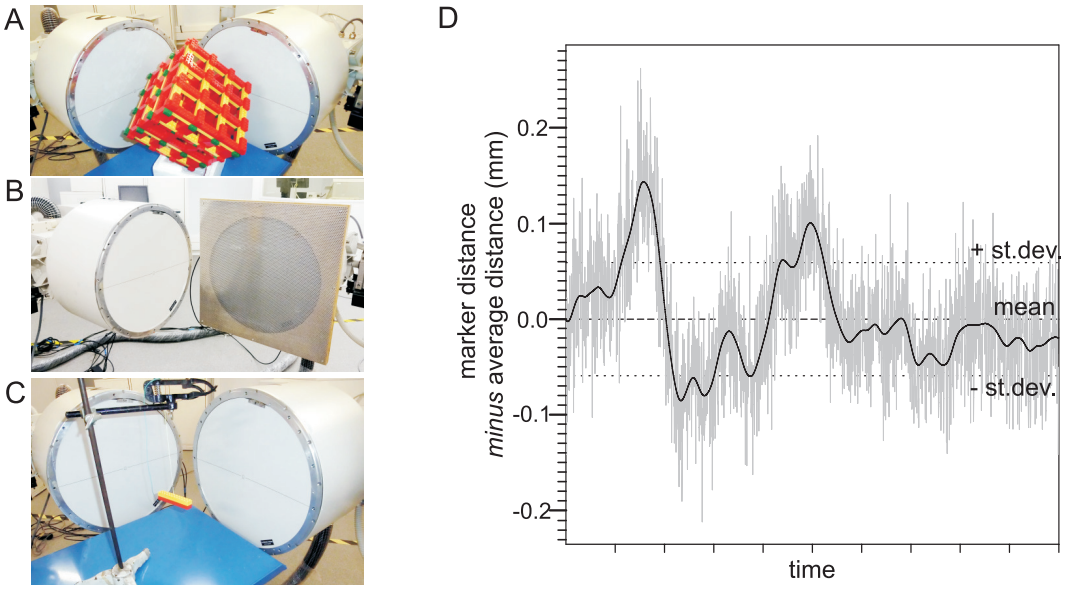

Figure 6. Precision of a dynamic measurement of fixed 3D distance (84 mm) between two metal spheres of 0.5 mm diameter following the XMAlab protocol. The Lego® calibration cube (A) described in Knörlein *et al* (2016) was used for calibrating the 3D scene. A planar, precision-punctured metal grid (B) was used to correct for spatial distortion of the image. The test object with the two metal spheres attached to the outer ends was rotated and swung about a wire attachment (C). The deviation from the mean in the calculated 3D distance between time-frames is displayed in (D).

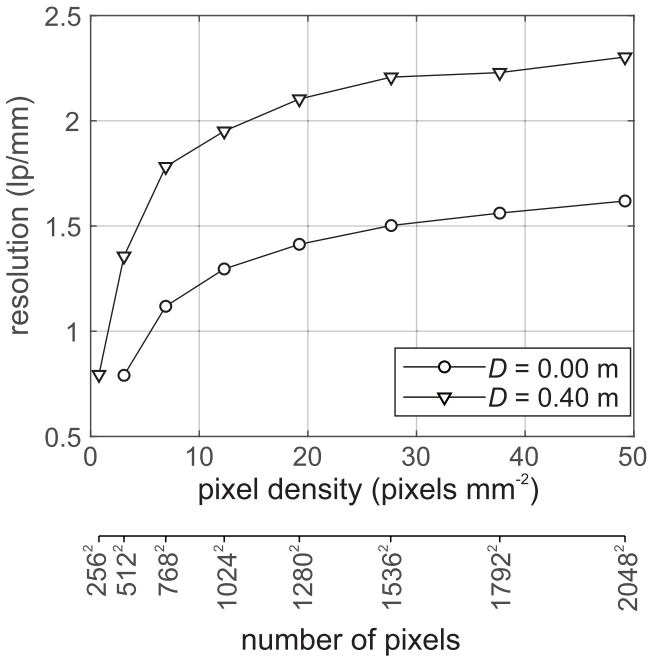

Figure 7. Effect of pixel density on spatial resolution of the high-speed camera images. Resolution corresponds to horizontal, line-pattern-based 10% MTF in large field of view mode. Results are shown for two distances (D) from the image intensifier screen: $D = 0.0$ (magnification factor 1), and $D = 0.4$ (magnification factor 1.67). A bicubic interpolation algorithm was used for image resampling.

divided by source-to-object distance) of approximately 1.25. Only accounting for the flat-fielded part of the image (see figure 2), the volumes were 8.1 dm^3, 2.6 dm^3, and 0.87 dm^3 for the large, medium, and small field settings, respectively. More information on the geometry of these volumes can be found in figure 4.

Resolution

First, the visually distinguishable resolution was determined for both image intensifiers for the three magnification settings, using the smallest focal spot, with the test pattern attached to the centre of the anti-scatter grid of the image intensifiers. The resolution for the large field of view differed slightly between the two image intensifiers; 2.2 line pairs mm^{-1} for image intensifier 1, and 2.5 line pairs mm^{-1} for image intensifier 2 (see also supplementary figure S1). At the other two magnification modes, resolution was consistent between the two image intensifiers, and was 3.4 and 4.6 line pairs mm^{-1} for the medium and small fields, respectively (figure S1). Second, edge-based 10% MTF resolutions were determined, which consistently yielded lower values (table 1). Note that 'horizontal resolution' R_h and 'vertical resolution' R_v correspond to the actual vertical and horizontal directions when the system is configured as shown in figure 1, which implies that R_v corresponds to the direction on the image intensifier that is parallel with the axis of the x-ray tube.

For the large field of view, we measured the effect of increasing the distance between the object and the image intensifier on 10% MTF resolution (figure 5). For the smallest focal spot setting, moving the test phantom away from the image intensifier (figure 5(A)) significantly increases the resolution (figures 5(B) and (C)). The line-pattern-based 10% MTF graph (figure 5(B)) indicates that the effect of object distance on resolution differs between the directions: horizontal resolution reaches a (higher) peak at 0.45 m (magnification factor 1.82), while vertical resolution is maximal at 0.3 m (magnification factor 1.43) from the image intensifier. The edge-based 10% MTF graph (figure 6(C)) shows a considerably smaller difference between horizontal and vertical resolutions. For both resolution metrics, overall 2D resolution for the small focal spot images is above 95% of the maximum achievable resolution at distances between 0.25 m and 0.54 m from the image intensifier (magnification factors between 1.33 and 2.20).

For the largest focal spot setting, the highest resolution was measured considerably closer to the image intensifier compared to the small focal spot (figures 5(B) and (C)). This optimum is reached at 0.15 m (magnification factor 1.18). The effect of object distance on large focal spot resolution is similar for both pixel directions (i.e. horizontal and vertical). The resolution drops below 95% of the maximum at a distance of 0.27 m (magnification factor 1.35) and 0.23 m (magnification factor 1.27), for, respectively, the line-pattern-based and the edge-based 10% MTF resolutions (figures 5(B) and (C)).

Precision of marker tracking

After calibration (figure 6(A)), and accounting for image distortion (figure 6(B)), distances between two markers on a moving rigid object (figure 6(C)) calculated based on raw 3D position data of automated marker tracking in XMALab varied by ± 0.236 mm (total value range), with a standard deviation of 0.066 mm. After low-pass filtering of the raw data (cut-off frequency in a fourth-order recursive butterworth filter of 1/100 of the frame rate), the total variation range was $\pm$ 0.114 mm, with a standard deviation of 0.050 mm (figure 6(D)).

Discussion

Our results confirm the sub-millimeter precision of marker-based routines documented for a similar biplanar high-speed x-ray video system in concert with XROMM software tools for calibration, distortion correction, and automated marker tracking: the standard deviation of a fixed-distance test case on the $3D^2YMOX$ system of 0.066 mm (figure 6) was in between the values reported previously for a manually moved wand (0.046 mm) and those for a variety pairwise distances of markers on a given skeletal element during *in vivo* motions (0.083 mm) recorded on a system at Brown University (Brainerd *et al* 2010). Similar to our results, the latter study also observed an improvement in precision of about 25% by filtering out the high-frequency noise in the data. As the pixel size at the largest field of view for an object under 1.25 magnification factor (e.g. at 0.2 m from the image intensifier with the source at 1 m) is 0.114 mm (=233.6 mm divided by 2048 pixels), one pixel inaccuracy in the frame-by-frame automated

detection of the centre of the spherical markers is probably responsible for this relatively large band of high-frequency noise (grey lines in figure 6).

The flat-fielding functionality of the Photron cameras significantly improved the image quality of the system. The Philips Imagica image intensifier and downstream optics showed a considerable variation in the intensity across the x-ray images (figure 2(A)), and also between the two image intensifiers (probably due to variation in the production process which includes manual administering of the scintillator layer). This could cause impaired image contrast and reduced marker tracking performance. Especially in case of locally oversaturated or undersaturated regions of the camera sensor, traditional subtraction of x-ray images from empty scenes (i.e. *a posteriori* flat-field correction) is no longer effective. By *a priori* performing this flat-fielding using Photron's pixel gain correction, a uniform intensity is achieved (except for the edges) (figure 2(B)). In this way, potential problems with local intensity differences are avoided, and a uniform dynamic range of the camera across the image is achieved.

An important aspect of image quality is spatial resolution. This will, for example, determine the minimal size of structures that can be discerned on the images. The visually distinguishable resolution values reported for our system (2.5 line pairs mm^{-1} at large field setting) are higher than those reported for the Keck Foundation XROMM Facility at Brown University (2 line pairs mm^{-1}; Miranda *et al* (2011)) of which the image intensifier has a similar entrance field size of 36 cm. Since the measured visually distinguishable resolution of 2.5 lp mm^{-1} is below the value of 3.1 lp mm^{-1} measured by the constructor on 100 mm film of our image intensifiers, the high-speed x-ray imaging chain is limited by the resolution of the high-speed camera. The slightly higher resolution of the $3D^2YMOX$ compared to the Keck XROMM is probably due to its higher pixel density: about 49 pixels mm^{-2} (2048 pixels per 292 mm; note that not the full circle is imaged as shown in figure 2) versus 25 pixels mm^{-2} of the Brown University system (1800 pixels per 360 mm). Note that resolution does not scale linearly with the number of pixels: downsampling our images to a (currently) more standard resolution for high-speed cameras of 1024 by 1024 pixels (1/4 of the original pixel density) reduces the horizontal 10% MTF resolution from 1.62 to 1.30 line pairs per mm. Consequently, an increase in resolution of about 25% can be expected from upgrading older systems with newer 4 megapixel cameras.

Knowing how resolution is affected by the position of the object between the detector and source is of high importance for optimizing the design of biplanar x-ray set-ups. However, to our knowledge, results of formal test of resolution in function of magnification factor (source-detector distance divided by source-object distance) are not available for high-speed x-ray systems equipped with high-resolution cameras. Resolution in the object's plane theoretically increases with magnification factor, but will be negatively affected by blur. As described in the review article by Schueler (1998), blur depends on focal spot size, and on the thickness of the caesium–iodide scintillator layer of the input screen (so-called 'receptor blur' due to the spreading of light photons formed by x-rays interacting with the intensifying screen), and on the magnification factor (influencing both 'receptor blur' and 'focal spot blur'). As Philips image intensifiers have relatively thin caesium–iodide layers of approximately 0.3 mm that are deposited in evaporated form during construction (van der Eijk and Kühl 1984), receptor blur is minimal (Schueler 1998), and the remaining focal spot blur will increase with increasing magnification factor.

Our measurements quantified the resultant of these opposing effects of blur and magnification on resolution in the object's plane, and showed that for the small focal spot setting, the optimal resolution is achieved at magnification factors between 1.33 and 2.20, with a peak at about 1.82 (figures 5(B) and (C)). For a typical set-up with the source at 1 m from the input screen, this corresponds to centering the subject about 0.45 m away from the image intensifier. If the object-detector distance needs to be larger than 0.6 m, it is recommended to place the source further back. If the large focal spot setting needs to be used, for example when higher tube currents and voltages are needed than achievable with the small focal spot, it is recommended to position the subject as close as possible to the image intensifiers to obtain the highest possible image quality.

To optimize the placement or orientation of the x-ray source and image intensifier in a biplanar x-ray set-up, it is worthy to consider the direction for which the highest resolution is desired. For magnification factors of 1.4 (object at 0.25 m with source at 1 m from the image intensifier) and higher, our system showed a considerably reduced resolution in the direction of the axis of the x-ray tube (figure 5(B)). This is most probably due to the approximately rectangular shape of our x-ray tube's small focal spot, which is about 20% larger in the direction of the tube axis. This would explain the increased focal spot blur, and resultant resolution loss along the tube axis direction. It is noteworthy that this effect is considerably less resolved when modulation transfer functions are derived without using the line-pair phantom: using the more common method to quantify resolution by analyzing gray value profiles at sharp edges (Judy 1976, Samei *et al* 1998), the differences in resolution between the two directions are considerably smaller (compare small FS traced in figures 5(B) vesus (C)). The reason for this is unclear to us, and may deserve attention in future studies.

Conclusion

When designing an experimental set-up for high-speed stereoscopic x-ray videography of moving organisms or body parts, many factors should be considered to optimise image quality. Some decisions are relatively straightforward, such as the choice of a sufficiently high frame rate to obtain useful kinematic profiles, or the choice of a sufficiently high shutter speed to reduce motion blur. The effect of other factors is more difficult to estimate, and trade-offs with each other. We showed how the interplay between focal spot blur and magnification of the x-rayed subject in the cone-beam affects image resolution (figure 5). Although the principles behind both

effects are well known (e.g. reviewed in Schueler (1998) and Bushong (2017)), such a quantification is novel for this type of system. It may help researchers to account for this effect when deciding on the distance between source and image intensifier, and at which location the subject should move, to have the highest possible image resolution while still monitoring a sufficiently large 3D volume to include the full motion of interest. Additionally, it should be kept in mind that the orientation of the x-ray source can be important under certain conditions, as focal spot asymmetry can cause significant asymmetry in the spatial resolution of the images (figure 5(B)). We also showed that images can be optimised using features of the newest generation of high-speed cameras: how pixel-based calibration can improve the dynamic range of the images (figure 2), and how a higher pixel density of the mounted high-speed camera can improve the resolution of the x-ray images (figure 7).

Acknowledgments

This study was funded by a grant from the Flemish Government (Hercules Foundation Grant No. AUHA/13/001), a grant from the special research fund of the University of Antwerp (BOF-GOA 2016 33927), and a grant from the French National Research Agency (Grant No. ANR-16-ACHN-0006-01).

ORCID iDs

J G Sanctorum https://orcid.org/0000-0002-9753-031X
D Adriaens https://orcid.org/0000-0003-3610-2773
J Sijbers https://orcid.org/0000-0003-4225-2487
S Van Wassenbergh https://orcid.org/0000-0001-5746-4621

References

Brainerd E L, Baier D B, Gatesy S M, Hedrick T L, Metzger K A, Gilbert S L and Crisco J J 2010 X-ray reconstruction of moving morphology (XROMM): precision, accuracy and applications in comparative biomechanics research *J. Exp. Zool.* **313A** 262–79

Bushong S C 2017 *Radiologic Science for Technologists: Physics, Biology, and Protection* 11th edn (St. Louis, MO: Elsevier)

Camp A L and Brainerd E L 2014 Role of axial muscles in powering mouth expansion during suction feeding in largemouth bass (*Micropterus salmoides*) *J. Exp. Biol.* **217** 1333–45

Camp A L, Astley H C, Horner A M, Roberts T J and Brainerd E L 2016 Fluoromicrometry: a method for measuring muscle length dynamics with biplanar videofluoroscopy *J. Exp. Zool.* A **325** 399–408

Du L Y, Umoh J, Nikolov H N, Pollmann S I, Lee T-Y and Holdsworth D W 2007 A quality assurance phantom for the performance evaluation of volumetric micro-CT systems *Phys. Med. Biol.* **52** 7087–108

Gatesy S M, Baier D B, Jenkins F A and Dial K P 2010 Scientific rotoscoping: a morphology-based method of 3D motion analysis and visualization *J. Exp. Zool.* **313A** 244–61

Geiger S M, Reich E, Böttcher P, Grund S and Hagen J 2018 Validation of biplane high-speed fluoroscopy combined with two different noninvasive tracking methodologies for measuring *in vivo* distal limb kinematics of the horse *Equine Vet. J.* **50** 261–9

Judy P F 1976 The line spread function and modulation transfer function of a computed tomographic scanner *Med. Phys.* **3** 233–6

Knörlein B J, Baier D B, Gatesy S M, Laurence-Chasen J D and Brainerd E L 2016 Validation of XMALab software for marker-based XROMM *J. Exp. Biol.* **219** 3701–11

Konow N, Cheney J A, Roberts T J, Waldman R S and Swartz S M 2015 Spring or string: does tendon elastic action influence wing muscle mechanics in bat flight? *Proc. R. Soc.* B **282** 20151832

Miranda D L, Schwartz J B, Loomis A C, Brainerd E L, Fleming B C and Crisco J J 2011 Static and dynamic error of a biplanar videoradiography system using marker-based and markerless tracking techniques *J. Biomech. Eng.* **133** 121002

Orsbon C P, Gidmark N J and Ross C F 2018 Dynamic musculoskeletal functional morphology: integrating diceCT and XROMM *Anat. Rec.* **301** 378–406

Samei E, Flynn M J and Reimann D A 1998 A method for measuring the presampled MTF of digital radiographic systems using an edge test device *Med. Phys.* **25** 102–13

Schueler B A 1998 Clinical applications of basic x-ray physics principles *RadioGraphics* **18** 731–44

Snelderwaard P C, De Groot J H and Deban S M 2002 Digital video combined with conventional radiography creates an excellent high-speed x-ray video system *J. Biomech.* **35** 1007–9

van der Eijk B and Kühl W 1984 An x-ray image intensifier with large input format *Philips Tech. Rev.* **41** 137–48

Wachs K, Fisher M S and Schilling N 2016 Three-dimensional movements of the pelvis and the lumbar intervertebral joints in walking and trotting dogs *Vet. J.* **210** 46–55

Wang J and Blackburn T J 2000 X-ray image intensifiers for fluoroscopy *RadioGraphics* **20** 1471–7

Yang L and Huiyan Z 1996 Shape preserving piecewise cubic interpolation *Appl. Math.* **11** 419–24